Journal Name

ARTICLE TYPE

Cite this: DOI: 10.1039/xxxxxxxxxx

Graphene growth by molecular beam epitaxy: an interplay between desorption, diffusion and intercalation of elemental C species on the islands†

Francesco Presel,[a] Holly Tetlow,[b] Luca Bignardi,[c] Paolo Lacovig,[c] Cristian A. Tache,[a‡] Silvano Lizzit,[c] Lev Kantorovich,[b] and Alessandro Baraldi*[acd]

Received Date
Accepted Date

DOI: 10.1039/xxxxxxxxxx

www.rsc.org/journalname

The growth of graphene by molecular beam epitaxy from an elemental carbon precursor is a very promising technique to overcome some of the main limitations of the chemical vapour deposition approach, such as the possibility to synthesize graphene directly on a wide variety of surfaces including semiconductors and insulators. However, while the individual steps of the chemical vapour deposition growth have been extensively studied for several surfaces, such a knowledge is still missing for the case of molecular beam epitaxy, even though it is a key ingredient to optimise its performance and effectiveness.

In this work, we have performed a combined experimental and theoretical study comparing the growth rate of the molecular beam epitaxy and chemical vapour deposition processes on the prototypical Ir(1 1 1) surface. In particular, by employing high-resolution fast X-ray photoelectron spectroscopy, we were able to follow the growth of both single- and multi-layer graphene in real time, and to identify the spectroscopic fingerprints of the different C layers. Our experiments, supported by density functional theory calculations, highlight the role of the interaction between different C precursor species and the growing graphene flakes on the growth rate of graphene. These results provide an overview of the main differences between chemical vapour deposition and molecular beam epitaxy growth and thus on the main parameters which can be tuned to optimise growth conditions.

1 Introduction

Even though the unique properties of graphene (Gr) make it an ideal candidate to replace silicon in nanoelectronic applications, its widespread adoption is still limited[1,2]. In addition, Gr-based materials such as graphene oxide and composites have shown great promise for the development of innovative photo- and electro-catalysts and gas sensors[3–7]. However, many applications of graphene require a very high crystalline quality of Gr, to ensure an outstanding performance and efficiency. The production of Gr with such characteristics is usually performed by chemical vapour deposition (CVD) on noble metal surfaces (usually polycrystalline Cu), followed by transfer onto its destination substrate[8]. This method, however, is not yet cost-effective[2]. Moreover, this transfer process introduces not only defects into the Gr sheet, but also contaminants such as metal atoms, which are incompatible with the requirements of nanoelectronic industry[9,10]. An approach which has been investigated to address these issues is to directly grow Gr on semiconductor or insulator surfaces. However, the CVD growth of Gr on such substrates requires very high temperatures as the surfaces are not able to efficiently catalyse the hydrocarbon precursor cracking, which has a significant impact on the Gr production costs[11–13].

The growth of Gr from atomic carbon sources, using the technologies of molecular beam epitaxy (MBE), is an alternative approach which does not require a hydrocarbon decomposition reaction, and therefore has proven a viable route to grow Gr on a wide variety of surfaces, including metals[14], semiconductors[11,12,15,16], insulators[10,17–24] and other 2D materials[25–28]. Moreover, it has proven effective in obtaining very high quality Gr on surfaces where CVD is successful, even at significantly lower growth temperatures than those required for the latter technique, thereby reducing production costs[14,16]. In addition, MBE from a

[a] Physics Department, University of Trieste, Via Valerio 2, 34127 Trieste, Italy. Tel: +39 040 3758719; E-mail: alessandro.baraldi@elettra.eu
[b] Physics Department, King's College London, London, WC2R 2LS, UK.
[c] Elettra-Sincrotrone Trieste S.C.p.A., Strada Statale 14 Km 163.5, 34149 Trieste, Italy.
[d] IOM-CNR, Laboratorio TASC, AREA Science Park, S.S. 14 km 163.5, 34149 Trieste, Italy.

† Electronic Supplementary Information (ESI) available: NEB calculations of carbon monomer and dimer diffusion on graphene. See DOI: 10.1039/b000000x/

‡ Present address: National Institute of Materials Physics, Atomistilor Str., No. 405A, 077125 Magurele, Romania.

solid evaporator is up to now the only successful technique in the synthesis of other 2D materials such as stanene, germanene and borophene[29–33].

However, in order to be able to fully exploit the advantages of this technique and optimise the growth conditions for increased cost-effectiveness and quality, an in-depth understanding of the growth process is required[34–36]. While several studies have explored the mechanisms of Gr growth by CVD on different surfaces[34,35,37–48], such a characterisation of the growth process is – to our knowledge – still missing for the case of MBE growth.

In this work, we have investigated the dynamics of MBE Gr growth by a combined experimental and theoretical approach based on X-ray Photoelectron Spectroscopy (XPS) and Density Functional Theory (DFT) calculations, in order to identify the most relevant parameters that regulate the process and can be most effectively exploited to improve the growth conditions. In particular, our aim was to highlight the most relevant differences between this technique and the more extensively employed CVD method. For this reason, we have chosen as a substrate the Ir$(1\,1\,1)$ surface, where the individual phases of the CVD growth process are already very well known, both experimentally[41,46,48] and theoretically[39,49,50].

In our work, we have used a high temperature growth approach for both the CVD and MBE techniques, by exposing the surface to the precursor at a temperature which is already sufficient for Gr growth[51]. This approach allows to study the dynamics of the flakes' accretion process in real time, in particular at the high-coverage limit. This latter phase represents a critical step in the growth process: in fact, at this stage, the metal surface directly exposed to the precursor is very limited, often consisting of 0D (mono- and di-vacancies) or 1D defects (grain boundaries and dislocations) of the graphene layer, which might not provide sufficient suitable adsorption sites for the precursor. This issue can lead to an incomplete Gr coverage, and the resulting uncovered areas and vacancies, besides lowering the electron mobility, represent a weak point from which Gr can be attacked by other reactive species[52]. On the other hand, on several substrates including Ir$(1\,1\,1)$, additional layers have been shown to form in some regions in particular conditions, especially at high precursor flux[37,38]. For these reasons, a good understanding of the dynamics of the last phases of the growth process is needed to ensure that the growth conditions lead to Gr with a controlled number of layers and a low density of defects.

Our experiments provide a spectroscopic characterisation of the single- and multi-layer Gr growth on Ir$(1\,1\,1)$. In particular, we show that high energy-resolution XPS allows to resolve the signal from the interface and upper layers of Gr. From real-time XPS measurements combined with *ab initio* theoretical calculations, we show that the MBE growth rate has a complex dependence on coverage, which is controlled by the interplay between the adsorption and diffusion of the carbon feedstock on the growing Gr flakes. This more complex kind of interplay, with respect to the CVD case, can be exploited to obtain either a single- (SL-Gr) or a multi-layer growth of Gr on this surface in a controlled and reproducible way: in fact, we show that the growth of a second layer only occurs after the surface has been fully covered by a complete SL-Gr. In addition, we prove that the MBE technique is self-limited to a certain Gr thickness. This is a consequence of the fact that the growth of the additional Gr layers occurs below the already formed ones[37], and therefore requires the intercalation of the C feedstock through them. These results highlight the key role played by the interactions between the precursors and the growing Gr flakes on the characteristics of the final product, and show that this parameter can be tuned by using different species of C atoms or small clusters (such as dimers) as precursors.

2 Experimental methods

The photoemission experiments were carried out in the ultra high vacuum chamber (base pressure 1×10^{-10} mbar) of the Super-ESCA beamline at the Elettra synchrotron radiation facility[53]. Photoemission spectra were collected using a Phoibos hemispherical electron energy analyzer from SPECS (150 mm mean radius), equipped with a delay-line detector. The experimental setup combines high energy resolution with high data acquisition rates, thus allowing real-time monitoring of the evolution of the core-level spectral components during processes such as gas exposure and temperature ramps[54]. The high-resolution core level spectra were acquired with photon energies of 400 eV for C $1s$ and 200 eV for Ir $4f_{7/2}$. The photon energy was chosen in order to maximise the photoionization cross-section and ensure a comparable mean escape depth for the photoelectrons of both spectral regions. In particular, at the chosen photon energies, about 60% of the signal arises from the first atomic layer. The overall experimental energy resolution, which accounts for both the electron energy analyzer and the X-ray monochromator, was kept within 50 meV for measurements in the range 200-400 eV. Doniach-Šunjić functions[55] convoluted to a Gaussian, with a Shirley-type background[56], were fitted to all the core level spectra to obtain the lineshape parameters and to determine the photoemission intensity and core level BE. The lineshape parameters of these functions describe the contributions due to the finite lifetime of the core-hole excited final state (Lorentzian FWHM, L), to the phonon-induced spectral broadening and experimental resolution (Gaussian FWHM, G), as well as to the electron-hole pair excitation probability (asymmetry parameter, α). The LEED experiments were carried out using a commercial VG instrument with a transfer width of about 100 Å.

The sample was heated by irradiation from hot W filaments mounted behind it. The temperature of the sample was monitored by means of two K-type thermocouples spot-welded on the sample. The Ir$(1\,1\,1)$ surface was prepared by using a well-established procedure[57], based on repeated cycles of sputtering, annealing and O_2 and H_2 treatments, which yields a long-range ordered and clean surface, as proven by the sharp and low-background (1×1) low energy electron diffraction (LEED) pattern and by the absence of traces of contaminants in the C $1s$, B $1s$, S $2p$ and O $1s$ core level regions.

Both the CVD and MBE growth were performed at a temperature of 1200 K, which is known to result in the formation of high-quality Gr on Ir$(1\,1\,1)$[41,51]. For the CVD growth, we performed several experiments by exposing the sample to different pressures of C_2H_4, ranging from 1×10^{-9} mbar to 1×10^{-7} mbar.

The carbon MBE growth was carried out by employing electron-beam bombardment on a high-purity graphite rod placed 80 mm from the sample surface, resulting in a carbon flux of 0.07 ML/s, as previously calibrated[58], where a monolayer (ML) is defined as C atoms/Ir unit cell. The quality of the Gr layer was verified from the LEED pattern, which exhibits extra spots around the zero- and first-order diffraction spots of the substrate, a clear fingerprint of a moirè structure due to the lattice mismatch between Gr and Ir (1 1 1). The moirè cell can be approximated as (10×10) Gr unit cells over (9×9) Ir unit cells, with a periodicity of 24.5 Å[59]. Inside each moirè cell, three different high-symmetry regions can be identified, whose names – FCC, HCP and TOP[60] – identify the non-equivalent adsorption sites of the centre of the C rings. While in the TOP region the Ir substrate atom lies right in the centre of the C ring, in the FCC and HCP regions the centre of the honeycomb lies on an Ir FCC and HCP site, respectively. It is important to underline that Gr/Ir (1 1 1) represents a prototype of a weakly interacting Gr layer[61].

3 Theoretical methods

In a previous work, we have shown that most of the C species that are produced by a Carbon source with our evaporation parameters are formed by monomers (C_1) and dimers (C_2)[58]. To investigate the role of these species on the growth rate and self-limiting behaviour of Gr growth, we have calculated the adsorption configuration and energy of these species on Gr. The DFT calculations of the carbon monomer and dimer adsorption on the Gr layer supported by the Ir (1 1 1) surface were performed using the CP2K code[62]. Goedecker-Teter-Hutter[63] pseudopotentials were used with the generalised gradient approximation and PBE exchange correlation functionals[64]. Van der Waals forces were included using the DFT-D3 method[65]. A fully optimised m-DZVP[66] basis set was used with a plane wave cut-off energy of 300 Ry. For geometry relaxations the forces on all atoms were less than 0.038 eV/Å. For the Gr/Ir (1 1 1) system a $(10 \times 10)/(9 \times 9)$ moirè cell was constructed, with the Gr sheet placed on 3 layers of Ir (1 1 1) and with a vacuum gap of 15 Å. The bottom layer was fixed to the bulk lattice constant and the upper two layers were allowed to relax. The adsorption energies are calculated from

$$E_{ads} = E_{C_{(1,2)}+Gr/Ir\,(1\,1\,1)} - E_{Gr/Ir\,(1\,1\,1)} - E_{C_{(1,2)}}$$

where $E_{C_{(1,2)}+Gr/Ir\,(1\,1\,1)}$ is the energy of the monomer or dimer adsorbed on Gr/Ir (1 1 1) and $E_{Gr/Ir\,(1\,1\,1)}$, $E_{C_{(1,2)}}$ are the energies of the Gr/Ir (1 1 1) system and monomer or dimer in the vacuum.

In addition, we calculated the diffusion barrier (E_{diff}) of C monomers and dimers on Gr/Ir (1 1 1) using the Climbing Image Nudge Elastic Band (CI-NEB) method[67]. The CI-NEB calculations were performed using 7 images.

4 Experimental results

Figure 1(a) shows the sequence of high resolution C 1*s* core level spectra measured *in situ* during C deposition from the carbon source at $T = 1200$ K. At the beginning of the uptake, a single component, A, is observed, at about 284.2 eV BE. With increasing C coverage, we observe a second component, B, appearing

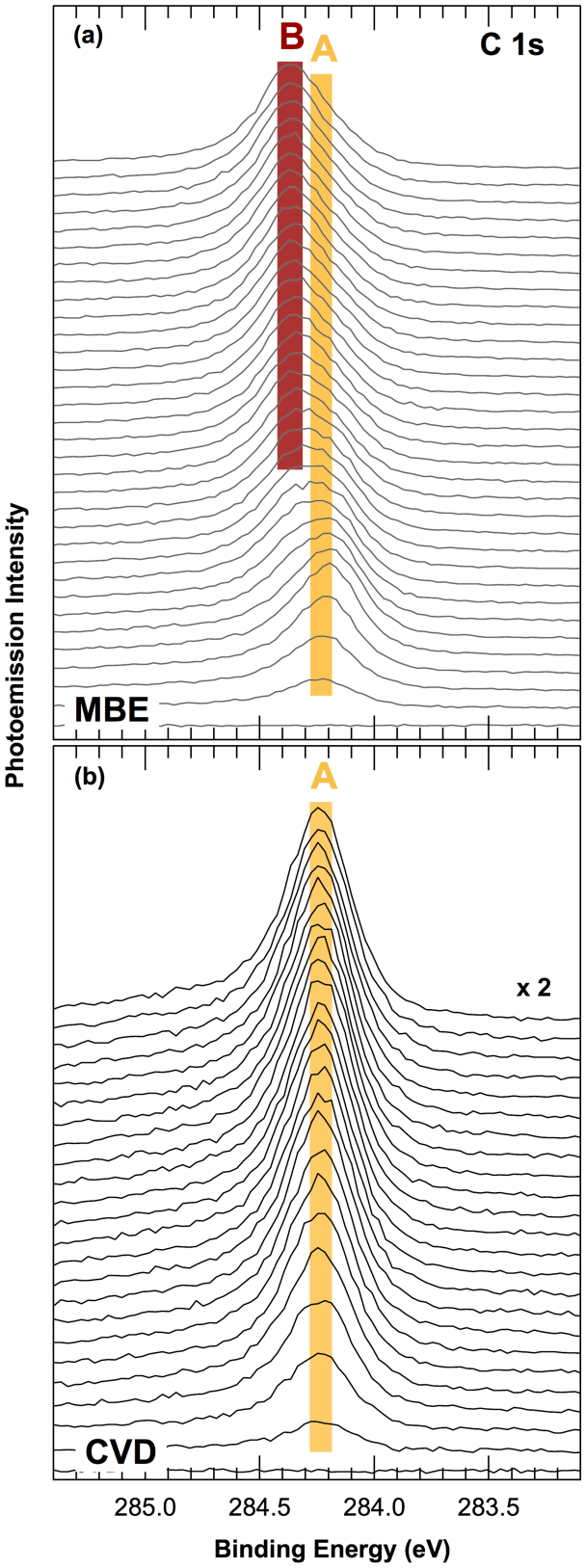

Fig. 1 Time-resolved C 1*s* spectra acquired during Gr growth on Ir (1 1 1) at 1200 K using the (a) MBE and (b) CVD (at 1×10^{-8} mbar C_2H_4) techniques.

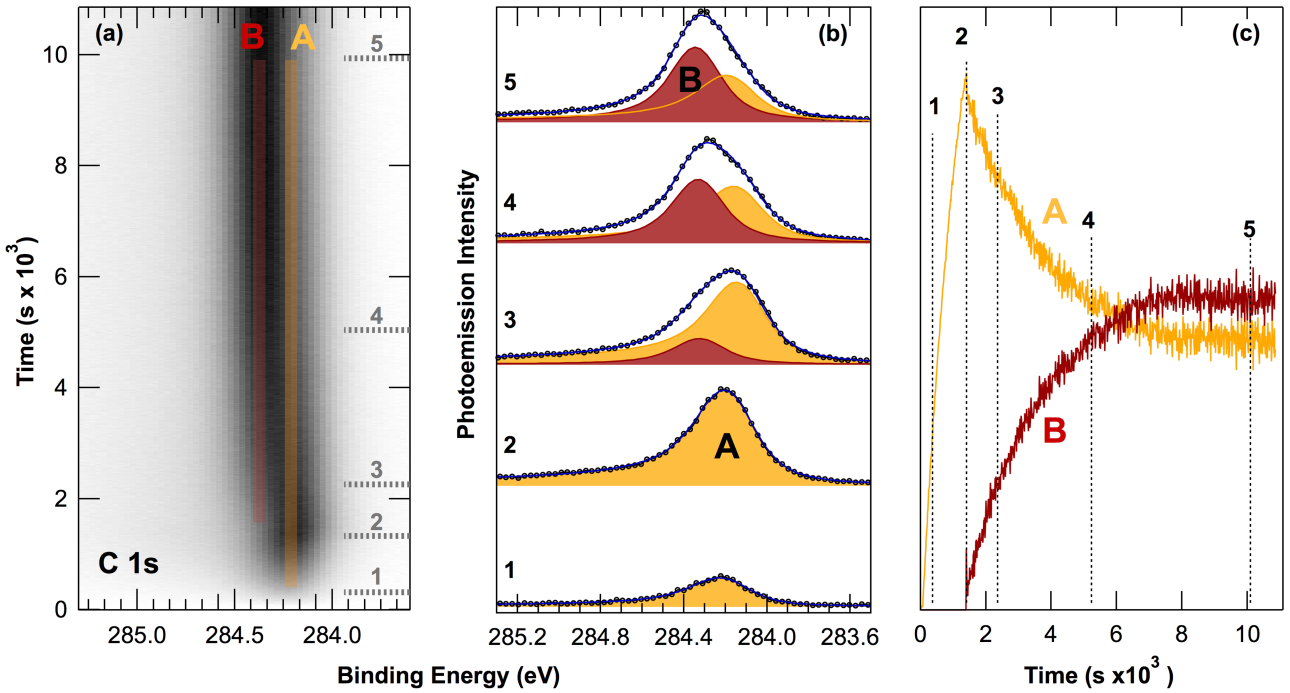

Fig. 2 (a) Time-resolved C 1*s* spectrum acquired during MBE growth at 1200 K. Selected spectra are plotted in (b), with their deconvoluted A and B components. (c) Evolution of the photoemission intensity of each spectral component.

at higher BE (284.35 eV), while the spectral weight of the low BE component decreases. This spectral series can be compared with the one measured during Gr CVD growth at the same temperature, during 1×10^{-8} mbar C_2H_4 exposure, which is shown in Figure 1(b). In the latter case, only a single component can be detected throughout the whole experiment, having the same BE as the A peak observed at the beginning of the MBE growth. This trend suggests that, while in the first stages of the growth the two methods produce the same C species, another non-equivalent C species appears at higher coverages only when depositing C from a solid target.

The modification in the C 1*s* spectral lineshape can be also appreciated in Figure 2(a), where the real-time spectra are reported as a two-dimensional plot in which the photoemission intensity is represented in grey scale, ranging from low (white) to high (dark). Representative spectra are shown in Figure 2(b) with their deconvoluted spectral components, A and B. More in detail, component A ($L = 200$ meV, $G = 180$ meV, $\alpha = 0.155$) was sufficient to properly describe the spectrum up to a coverage corresponding to that of a full SL-Gr on Ir (1 1 1), as obtained from the self-limiting CVD growth[41]. For higher coverage, instead, component B also had to be included. This latter peak has a lineshape characterised by $L = 215$ meV, $G = 150$ meV and $\alpha = 0.045$.

It is clear from Figure 2(c), where the intensities of the A and B components are plotted as a function of the carbon deposition time, that the intensity of component A decreases as component B increases. The evolution of the two components and the overall increase in C coverage suggest that the new B species originates from additional non-equivalent carbon atoms. As will be discussed later on, the C 1*s* binding energy value of the B peak, very close to the one measured on graphite[68], suggests that the new component could be attributed to a second and further layers of Gr located above the first Gr layer. In fact, the decrease in the intensity of the A component can be explained as due to the increasing attenuation of the photoemission signal of the interface carbon layer – the one directly above the Ir surface – exerted by the additional layers of carbon atoms lying above it. Based on these results, we believe that the single-layer growth is completed at the point indicated by 2 in Figure 2, after which multi-layer growth starts.

To quantitatively assess the total carbon coverage of multi-layer Gr (Figure 3(d)), we evaluated the attenuation of the photoemission signal of both the Ir $4f_{7/2}$ (Figure 3, left) and C 1*s* (Figure 3, right) core levels due to the limited mean free path of photoelectrons[69]. In particular, for the case of the C 1*s* (Figure 3(d), right), it is important to consider that not only the A component (which is attributed to the Gr interface layer, as will be described later) will be screened by the second and further layers, but also the total intensity of component B will be given by the sum of the contributions of each C layer, each screened by all the layers lying above it. This contribution, however, cannot be simply modelled since it requires the knowledge of whether the multi-layer Gr growth occurs by layers or by islands and, in the latter case, their average size. For this reason, an average number n of Gr layers has to be defined by taking into account their screening effect on the Ir $4f_{7/2}$ and C 1*s* photoemission signal. The number of additional Gr layers besides SL-Gr, *i.e.* excluding the one at the interface, is denoted as $m = n - 1$. More in detail, we calculated these numbers from the relations $I_A/I_{A,MAX} = a^m$ and $I_{Ir}/I_{Ir,0} = a^n$, where I_A is the intensity of the C 1*s* component A, I_{Ir} that of Ir $4f_{7/2}$ and

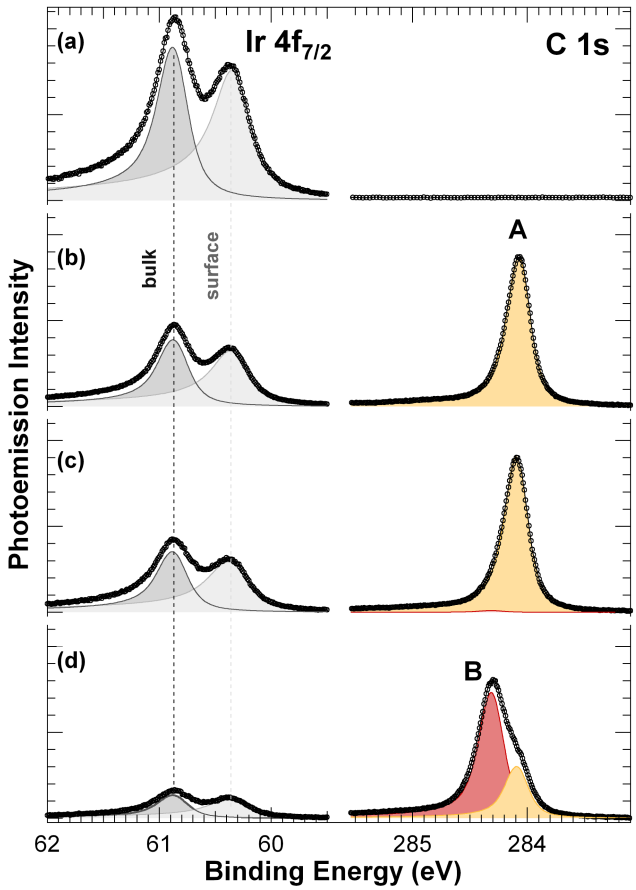

Fig. 3 Ir $4f_{7/2}$ (left) and C $1s$ (right) spectra acquired at 300 K on (a) clean Ir (1 1 1), and after (b) CVD growth of a single Gr layer, (c) MBE growth of a single Gr layer, and (d) growth of multi-layer Gr.

a is the attenuation by a single C layer. This latter parameter can be obtained by measuring the attenuation of the Ir $4f_{7/2}$ intensity when $n = 1$, *i.e.* the one due to SL-Gr as obtained from the CVD growth. As shown in Figure 3(a), left, both the surface and bulk components of clean Ir (1 1 1)[57] are indeed showing an intensity which is reduced by the same factor, corresponding to a parameter $a = 0.43$. It is interesting to notice that this is the same attenuation which is obtained from the growth using the C source, just before the second component starts to appear (Figure 3(c), left). Finally, the attenuation of the Ir $4f_{7/2}$ signal at the end of the experiment (Figure 3(d), left) is 0.16: by applying the same formula, this yields $n = 2.17 \pm 0.10$.

The right-hand part of Figure 3 shows instead the photoemission intensities of both C $1s$ components (A and B) in the same systems. In Figure 3(c), component A has the same intensity as the one obtained in the CVD experiment (Figure 3(b)) while component B is just 0.01 times as intense, which indicates that, at this stage, the interface Gr layer was complete and the growth of additional layers was just starting. On the other hand, in Figure 3(d), component A has decreased to 0.35 times its original intensity, while the intensity of B is 0.86 times that of the full SL-Gr in Figure 3(b), right. Based on these results, we calculated m also from the attenuation of the A component in the C $1s$ spectrum, obtaining a value $m = 1.24 \pm 0.10$, in very good agreement with the results obtained from the Ir $4f_{7/2}$ spectrum analysis. Based on the combination of these two methods, we estimate a value $n = 2.20 \pm 0.15$. As a full layer of Gr has a coverage of 2.47 ML, n can be related to the C coverage Θ by the relation $n = \Theta/2.47\,\mathrm{ML}$, yielding $\Theta = 5.43 \pm 0.40\,\mathrm{ML}$.

An important observation is that the ratio between the A and B components of C $1s$ in the spectra taken at high temperature (Figure 1) does not correspond to the one obtained from measurements at room temperature (Figure 3). This can be explained in terms of a modified mean free path which could be originated for instance by an enhanced electron-phonon scattering by Gr at high temperature, as demonstrated for the case of other solid surfaces[70]. Therefore, in order to calculate the C coverage for the real-time spectra of the uptake experiment, the following procedure was applied: as long as only component A was present, the coverage was considered proportional to its intensity. In the second part of the uptake, where component B was also present, the coverage of A was fixed to the maximum value it had reached, on the base of the growth model proposed above. To evaluate the coverage of the additional Gr layers, the same formulas were used as for the room temperature data; however, a new parameter $a_{1200\,\mathrm{K}}$ was introduced in place of a, corresponding to the value of the attenuation by SL-Gr at $T = 1200\,\mathrm{K}$. This parameter was calculated from the ratio between the final and maximum intensity reached by the A component during the uptake, by employing the coverage value obtained from the room temperature measurements (5.43 ML). This high-temperature attenuation parameter was then used to quantify the number m of C layers covering the interface one as a function of time.

We further characterised the system by acquiring LEED images corresponding to all systems described above, as reported in Figure 4. The SL-Gr prepared by CVD shows the well-known diffraction pattern[48], with the presence of several spots due to the formation of the long-range order periodicity of the moiré superlattice, which are aligned with those of the Ir (1 1 1) surface (Figure 4(a)). These spots, however, are much broader along a tangential than along a radial direction, thus indicating that Gr is not completely aligned with the substrate's crystallografic directions, but shows a narrow distribution of rotational domains around this direction. The presence of rotational domains in constant-temperature CVD-grown Gr on Ir (1 1 1) is indeed one of the main drawbacks when using this growth method on this surface[51]. On the other hand, the MBE growth (Figure 4(b)) of a single Gr layer leads to significantly narrower spots, which do not display an evident angular broadening; moreover, a higher number of diffraction orders can be seen. This indicates that for similar growth conditions, the constant-temperature MBE growth of SL-Gr on Ir (1 1 1) leads to a higher crystallographic quality of the product, in agreement with what has been observed on several other surfaces[14,16]. Finally, the image corresponding to the multi-layer formation (Figure 4(c)) still shows the same moiré spots, even though the background intensity has increased and they show an increased broadening, indicating an overall poorer crystallographic alignment and long-range ordering, and higher density of defects, in the multi-layer Gr.

Another interesting result obtained in the carbon MBE exper-

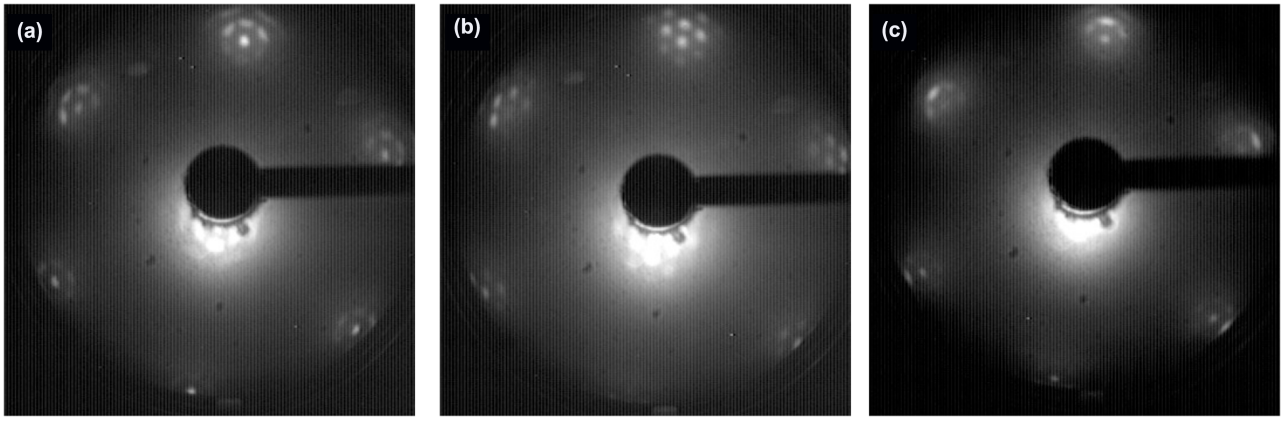

Fig. 4 LEED of single-layer Gr grown on Ir $(1\,1\,1)$ at 1200 K via CVD (a) and MBE (b) and after multi-layer Gr growth by MBE (c) ($E = 74$ eV).

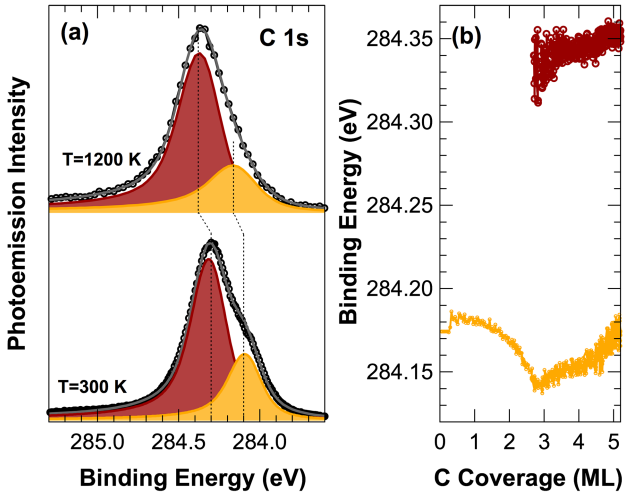

Fig. 5 (a): Comparison of C 1s core-level spectra of multi-layer Gr at growth temperature (above) and room temperature (below). (b): C 1s core-level BE evolution during MBE Gr growth at 1200 K.

iment can be appreciated in Figure 5(a), where the C 1s spectra of the A and B components measured at the end of the uptake at high temperature (T=1200 K) and at room temperature (T=300 K) are reported. At the end of the uptake, when about 2 Gr layers are present, the C 1s BE of A and B results to be about 284.17 eV and 284.38 eV respectively, as shown in the top spectrum of Figure 5(a). However, when the Ir $(1\,1\,1)$ crystal is cooled to room temperature, both components are characterized by a lower core level BE, which amounts to 284.10 eV and 284.30 eV, respectively (Figure 5(a), bottom). This decrease, of about 70 meV - 80 meV, can be explained as due to the positive thermal expansion of supported Gr, which is driven by that of the Ir substrate underneath. In particular, we compared our experimental findings with the C 1s core levels calculated by means of DFT and molecular dynamics simulations for free-standing and Ir $(1\,1\,1)$-supported Gr[71]. By increasing the temperature from 300 K to 1000 K, the calculated C 1s core level shifts of supported Gr increase by 70 meV, which is in very good agreement with the increase we observe in our data.

Furthermore, as shown in Figure 5(b), the C 1s BE of both components A and B shifts during the whole growth. In particular, before a full SL-Gr is formed, the BE of the only component (A) decreases progressively. The minimum BE of the interface GR layer, corresponding to the maximum degree of p-doping, is achieved when a full SL-Gr is present. The C 1s BE of both components, instead, increases when the multi-layers start forming, with a roughly linear dependence on coverage. In particular, for increasing number of layers, the C 1s BE of component B moves closer to the value found in bulk graphite, which is 284.4 eV[68].

5 Theoretical results

Figure 6 shows the calculated relaxed adsorption configuration of C monomers (C_1) and dimers (C_2) on Gr/Ir $(1\,1\,1)$.

The C monomer is found to be unstable in the hollow and atop positions in the Gr unit cell, and will tend to relax to the bridge configuration. We calculated the adsorption energy for C monomers sitting in this site in the different regions (TOP, HCP and FCC) of the Gr (10×10) unit cell, as shown in Figure 6(a). While the HCP-bridge and FCC-bridge configurations show quite similar adsorption energy values (2.37 and 2.38 eV, respectively), the TOP-bridge site is slightly preferred, with and adsorption energy of 2.48 eV. Also C dimers preferentially adsorb in TOP-bridge sites (Figure 6(b)), with a slightly larger adsorption energy of 2.60 eV. It is interesting to note that the dimer adsorbs with its axis perpendicular with respect to the Ir surface and induces a considerable local deformation in the Gr lattice, by lifting up the nearest- and next-nearest-neighbour C atoms. By comparing the two systems, it is clear that the adsorption energies of a C monomer or dimer are quite similar.

The pathway and energetics of the diffusion process are shown, for both species, in the Supporting Information. The most interesting finding is the much larger barrier E_{diff} found for the C monomers' diffusion from TOP-bridge to TOP-bridge sites (0.60 eV) with respect to the case of C dimers (0.26 eV - 0.28 eV, depending on the choice of the initial-state).

6 Discussion

The comparison between the evolution of the C coverage in the uptakes performed at the same temperature, using either the car-

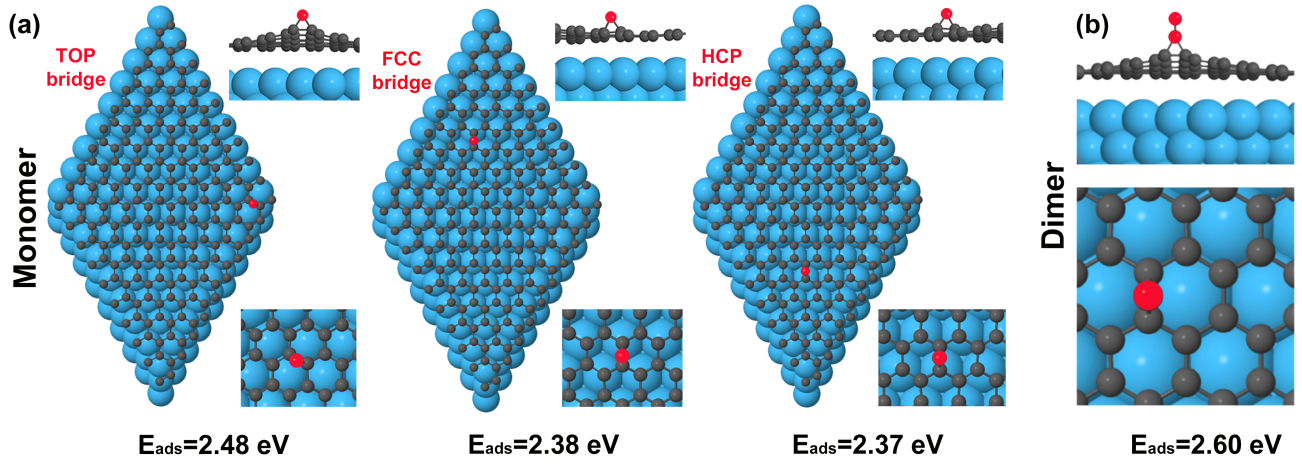

Fig. 6 Preferred adsorption configurations for (a) C_1 and (b) C_2 species on Gr supported on Ir(111). For the case of the monomers ((a)), the adsorption energy in non-equivalent regions of the Gr moirè supercell is shown.

bon source or ethylene CVD, is shown in Figure 7. In order to be

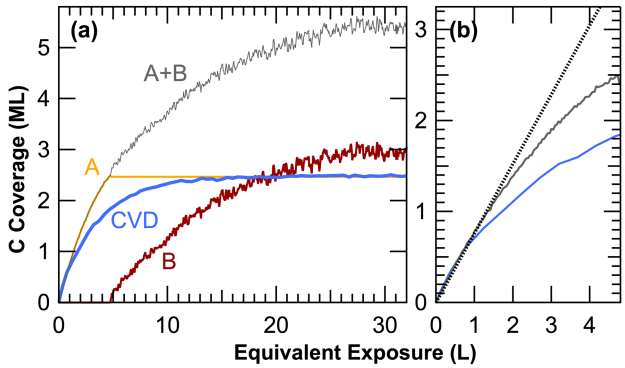

Fig. 7 Comparison of the growth rate of Gr during MBE and CVD at 1200 K at 1×10^{-8} mbar C_2H_4. In (a), the total coverage of CVD- and MBE-grown Gr are shown, together with the individual coverage of the first and upper layers. (b): zoom-in of the initial growth rate and comparison with a linear behaviour (dashed).

able to compare the two different methods, however, it was firstly necessary to correctly align the reaction coordinate for the two experiments, namely the atomic carbon flux on the sample and the exposure of the surface to the gas precursor respectively. This was achieved by imposing a matching of the first derivatives of the photoemission intensity curves with respect to the exposure coordinate in the low-coverage region (*i.e.* below 0.1 ML). This strategy is based on the approximation that at the early stage of Gr nucleation the change in the coverage depends mainly on the C supply rate (either from C_2H_4 molecules or from monomers/dimers originating from the source) and not on the specific structures present on the surface[35,41].

As shown in Figure 7(a), the two curves corresponding respectively to C 1*s* component A in MBE (orange) and to the corresponding single component in CVD (blue) reach the same maximum intensity, which corresponds to a coverage of 2.47 ML. However, the rate at which this maximum is reached is very different: while that of the CVD process gradually decreases and the approach to the 2.47 ML limit is asymptotic with coverage, the growth rate is still close to its initial value when the coverage reaches that value for the MBE case. This difference can be appreciated in particular starting from a coverage of 1 ML, when the slope of the curve corresponding to the CVD growth experiment is clearly decreasing with respect to the C-source experiment, as highlighted in the zoom-in shown in Figure 7(b).

The asymptotic behaviour is a clear fingerprint that, in the CVD process, the growth rate depends on the portion of the surface which is still free from Gr. As previously reported[41], this can be attributed to the very weak interaction between the regions already covered by Gr and the precursor C_2H_4 molecules, which causes the molecules adsorbing there to immediately desorb, without generating carbon feedstock. This is at the base of the already mentioned self-limiting behaviour of CVD-grown Gr on Ir(111), which allows to obtain SL-Gr with excellent selectivity on this surface. On the other hand, the Gr growth rate for the MBE process does not vanish at a coverage of a full Gr layer, and the total coverage increases further, as the new photoemission component B grows. It is interesting to point out that the growth of the B peak starts exactly after the A component has reached its maximum. This indicates that while the MBE growth is not self-limiting and causes multi-layer growth, it is still possible to selectively obtain either SL-Gr or thicker Gr films by carefully monitoring the deposition process.

However, there is a limit to the thickness which can be obtained by using this technique: the growth of the additional layers, shown in Figure 7(a), eventually does reach saturation, which in our conditions is reached after an equivalent exposure of about 30 Langmuir of carbon and at a coverage slightly higher than 2 full C layers. The capability to distinguish between interface (A) and additional (B) Gr layers in the C 1*s* spectrum allows us to rule out possible artifacts in the evolution of their photoemission signal due to the limited mean free path of electrons – which could lead to an apparent saturation effect on the total C 1*s* signal –. Since not only their total intensity, but also their spectral weight does not vary any longer (as can be seen in Figure 2(c)), we can conclude that the growth has really stopped. This is quite surprising, as one would expect the sticking probability not to vary signifi-

cantly any more once the whole surface is covered by Gr. Another remarkable result can be appreciated by observing the LEED pattern generated by the Gr multi-layer, shown in Figure 4(c), which still shows that the Gr layer is quite well aligned to the Ir (1 1 1) substrate. A high degree of orientational ordering between CVD- or MBE-grown Gr and its substrate is usually only observed when there is a high degree of interaction between the C feedstock and the substrate. For example, Gr has very few preferential orientations on strongly interacting surfaces such as Re (0 0 0 1) [72] and Ru (0 0 0 1) [73], can display several rotational domains on surfaces such as Ir (1 1 1) [51] and Rh (1 1 1) [74], and often shows no preferred orientation on very weakly interacting ones such as Pt (1 1 1) [75,76] and Au (1 1 1) [14]. According to this, Gr is expected to show very poor rotational alignment when growing on top of another Gr layer [38], and therefore the appearance of ring-like diffraction features in the LEED pattern would be likely, as in the case of highly oriented pyrolytic graphite [77,78]. These two remarkable facts can both be explained if the growth of the new C layers takes place not on top of the already grown layers, but on the buried Ir (1 1 1) surface, by intercalation of C monomers/dimers at the interface between the SL-Gr and the Ir substrate. This behaviour, indeed, has been already observed in LEEM experiments on the Ir (1 1 1) surface [37] and on other surfaces such as Cu (1 1 1) [38]. The progressive reduction in the rate of multi-layer growth, then, can be attributed to the fact that as further layers grow, it becomes increasingly difficult for the C atoms to intercalate and reach the surface, which is required to continue the growth. Moreover, the growth of the new layers, since it occurs on the Ir (1 1 1) surface, is still driven in its crystallographic direction by the interaction of the precursors with it.

It is interesting to notice that, in our case, we were able to obtain a multi-layer Gr where all layers have a reduced orientational disorder, being narrowly distributed around a direction parallel to the substrate's lattice vectors. Previous studies by Nie *et al.* [37], on the other hand, which were performed by depositing additional elemental carbon on a full CVD-grown Gr layer/Ir (1 1 1) characterised by multiple rotational domains, showed that the growth of a second layer was very rare below Gr oriented parallel to the substrate crystallographic axes, when compared to the case of the rotated Gr domains.

Finally, it is evident from Figure 7(b) that the growth rate of the first Gr layer by MBE is still influenced by the amount of free metallic surface, even though not as dramatically as in CVD. In fact, while the growth rate remains relatively large, it is nevertheless decreasing at high coverage (starting approximately above 1 ML), reaching about 80% of its initial value when the coverage approaches that of a full Gr layer (Figure 7(a)). This decrease must be related to some process occurring on the surface, similar to the self-limiting behaviour occurring in the CVD growth process yet less dramatic. For the case of CVD, in fact, the reduction in the growth rate is due to the very low residence time of the gaseous precursors on the Gr flakes, which causes them to desorb before they can participate in the growth. The MBE behaviour, instead, can be explained by the fact that the carbon monomers and dimers have an adsorption energy on Gr which is large enough to allow their adsorption on the surface and diffusion for a certain distance across the Gr flakes, yet the desorption probability is still not negligible. This leads to an interplay between these two processes: the carbon species adsorbed close enough to the flakes' edges can diffuse and reach them in a time shorter than their average residence time on the surface, while those farthest from them will desorb with high probability before they can reach them.

More in detail, we used the results from our theoretical calculations to quantitatively assess this hypothesis. In particular, the time required for the adsorbed carbon to desorb from Gr is $\tau_{ads}(T) \propto e^{E_{\text{ads}}/k_B T}$, which will be larger than the one required to move to an adjacent cell, $\tau_{diff,1}(T) \propto e^{E_{\text{diff}}/k_B T}$, where k_B is the Boltzmann constant and T is the temperature. Moreover, the average time required to diffuse across N unit cells is simply N times that required to move to an adjacent cell: $\tau_{diff,N}(T) \propto N e^{E_{\text{diff}}/k_B T}$. By equalling these two quantities, we can obtain the maximum number of Gr unit cells N_{MAX} which an adsorbate can diffuse through before desorbing. Finally, if we assume that the diffusion of the adsorbates does not have any preferred direction, the cells crossed by the adsorbates define an area, rather than a straight line, on the surface, and therefore the average distance travelled by the adsorbates is proportional to the square root of N_{MAX}:

$$r_{\text{MAX}} = a_{\text{GR}} \sqrt{N_{\text{MAX}}}$$

where a_{GR} is the lattice parameter of Gr. The values thus obtained for the monomers and dimers are respectively $r_{\text{MAX},M} = 2.4\mu$m and $r_{\text{MAX},D} = 18.3\mu$m. For each carbon species, this value defines the radii of two zones inside the Gr islands growing on the Ir (1 1 1) surface. In particular, for the case of monomers, those flakes whose radius is larger than the $r_{\text{MAX},M}$ have an inner and an outer region, separated by a boundary located at a distance $r_{\text{MAX},M}$ from the edge, such that carbon monomers deposited in the outside region participate to the flakes' growth, as they manage to diffuse until the edge of the flake, while those deposited in the inside region desorb before they can reach an edge. Likewise, a different boundary, at a distance of $r_{\text{MAX},D}$ from the islands' edge, separates the region where deposited dimers can participate in the growth or not. Due to the different values of $r_{\text{MAX},M}$ and $r_{\text{MAX},D}$, the islands of intermediate size between these values have two regions: the outer one, where both monomers and dimers can reach the edge, and the inner one, where only dimers can migrate to the edges. For even larger islands, a third, innermost region is present, where no deposited species is able to participate in the growth.

This mechanism very well explains the observed curve of the growth rate. In fact, for low carbon coverage, the islands size is smaller than the diffusion limit of both carbon species, and the growth rate is constant as all adsorbed C species participate to the growth, regardless whether they are deposited on an already nucleated Gr flake or on a bare region of the surface. Only at high coverages, when extended regions of the surface are covered by Gr, a decrease in the growth rate is observed. In our system, the growth is fed by monomers and dimers in a fairly similar ratio [58] and the reduction we observe in the growth rate is about 20%: we can calculate from this that the decrease we observe is almost

exclusively due to the monomers, and that the average size of the Gr islands, at a coverage approaching that of a full Gr layer, is between 5 and 10 μm. This size is comparable to the average distance between nucleated islands reported in LEEM experiments during CVD growth on the same surface[41]. It is important to observe that this size is not necessarily coincident with the average distance between grain boundaries, as a single island could be formed by several grains, as long as there is no free iridium surface in between.

7 Conclusions

In this work, we have described an investigation of the factors governing the growth of Gr by means of MBE carbon deposition from a solid evaporator. In particular we have shown that both single-layer and multi-layer Gr can be grown by deposition of carbon monomers and dimers on the Ir(1 1 1) surface. For the case of SL-Gr, a high quality and remarkable rotational alignment with the crystal vectors of the substrate can be achieved at lower temperature (1200 K) with respect to the CVD growth[51]. In addition, we have shown that this technique allows to obtain multi-layer Gr characterised by a very narrow angular distribution of its different layers. Most importantly, by analysing the growth rate, we have shown how the growth kinetics are controlled by a complex interplay between the diffusion of the C precursors on the growing Gr islands and their desorption. This interplay is controlled by the size of the islands and strongly depends on the chemical species composing the carbon feedstock: this fact provides an additional degree of freedom, besides temperature, to tune both the quality of the Gr and the number of layers grown, by modifying the composition of the carbon feedstock delivered.

The simple working principles of this technique, which unlike CVD does not require any catalytic reactions, make it an ideal tool for the growth of Gr or other 2D materials on a wide variety of substrates. Another possible advantage of the MBE technique is the possibility to produce Gr-based heterostructures or components with an arbitrary shape for use in electronic devices by shadow masking techniques[79]. Our results provide a generic overview of the factors which play the most important role on the growth dynamics, thus indicating the growth parameters which can be most effectively tuned in order to improve the quality of MBE-grown materials and to reduce production costs.

Conflicts of interest

There are no conflicts to declare.

Acknowledgements

Through membership of the UK's HPC Materials Chemistry Consortium, which is funded by the EPSRC (grant EP/L000202), this work made use of the facility of ARCHER, the UK's national high performance computing service, which is funded by the Office of Science and Technology through the EPSRC's High End Computing Programme.

Notes and references

1 A. Zurutuza and C. Marinelli, *Nat. Nanotechnol.*, 2014, **9**, 730–734.

2 A. C. Ferrari, F. Bonaccorso, V. Fal'ko, K. S. Novoselov, S. Roche, P. Bøggild, S. Borini, F. H. L. Koppens, V. Palermo, N. Pugno, J. A. Garrido, R. Sordan, A. Bianco, L. Ballerini, M. Prato, E. Lidorikis, J. Kivioja, C. Marinelli, T. Ryhänen, A. Morpurgo, J. N. Coleman, V. Nicolosi, L. Colombo, A. Fert, M. Garcia-Hernandez, A. Bachtold, G. F. Schneider, F. Guinea, C. Dekker, M. Barbone, Z. Sun, C. Galiotis, A. N. Grigorenko, G. Konstantatos, A. Kis, M. Katsnelson, L. Vandersypen, A. Loiseau, V. Morandi, D. Neumaier, E. Treossi, V. Pellegrini, M. Polini, A. Tredicucci, G. M. Williams, B. H. Hong, J.-H. Ahn, J. M. Kim, H. Zirath, B. J. van Wees, H. van der Zant, L. Occhipinti, A. Di Matteo, I. A. Kinloch, T. Seyller, E. Quesnel, X. Feng, K. Teo, N. Rupesinghe, P. Hakonen, S. R. T. Neil, Q. Tannock, T. Löfwander and J. Kinaret, *Nanoscale*, 2015, **7**, 4598–4810.

3 N. Zhang, M.-Q. Yang, S. Liu, Y. Sun and Y.-J. Xu, *Chem. Rev.*, 2015, **115**, 10307–10377.

4 M.-Q. Yang, N. Zhang, M. Pagliaro and Y.-J. Xu, *Chem. Soc. Rev.*, 2014, **43**, 8240–8254.

5 M.-Q. Yang, C. Han, N. Zhang and Y.-J. Xu, *Nanoscale*, 2015, **7**, 18062–18070.

6 G. Lu, L. E. Ocola and J. Chen, *Nanotechnology*, 2009, **20**, 445502.

7 M. Pumera, A. Ambrosi, A. Bonanni, E. L. K. Chng and H. L. Poh, *TrAC, Trends Anal. Chem.*, 2010, **29**, 954–965.

8 X. Li, Y. Zhu, W. Cai, M. Borysiak, B. Han, D. Chen, R. D. Piner, L. Colombo and R. S. Ruoff, *Nano Lett.*, 2009, **9**, 4359–4363.

9 J. Kang, D. Shin, S. Bae and B. H. Hong, *Nanoscale*, 2012, **4**, 5527–5537.

10 G. Lupina, J. Kitzmann, I. Costina, M. Lukosius, C. Wenger, A. Wolff, S. Vaziri, M. Östling, I. Pasternak, A. Krajewska, W. Strupinski, S. Kataria, A. Gahoi, M. C. Lemme, G. Ruhl, G. Zoth, O. Luxenhofer and W. Mehr, *ACS Nano*, 2015, **9**, 4776–4785.

11 G. Wang, M. Zhang, Y. Zhu, G. Ding, D. Jiang, Q. Guo, S. Liu, X. Xie, P. K. Chu, Z. Di and X. Wang, *Sci. Rep.*, 2013, **3**, 2465.

12 J. Dabrowski, G. Lippert, J. Avila, J. Baringhaus, I. Colambo, Y. S. Dedkov, F. Herziger, G. Lupina, J. Maultzsch, T. Schaffus, T. Schroeder, M. Kot, C. Tegenkamp, D. Vignaud and M.-C. Asensio, *Sci. Rep.*, 2016, **6**, 31639.

13 S. Gottardi, K. Müller, L. Bignardi, J. C. Moreno-López, T. A. Pham, O. Ivashenko, M. Yablonskikh, A. Barinov, J. Björk, P. Rudolf and M. Stöhr, *Nano Lett.*, 2015, **15**, 917–922.

14 I. Hernández-Rodríguez, J. M. García, J. A. Martín-Gago, P. L. de Andrés and J. Méndez, *Diamond Relat. Mater.*, 2015, **57**, 58–62.

15 J. Tang, C. Kang, L. Li, W. Yan, S. Wei and P. Xu, *Physica E*, 2011, **43**, 1415–1418.

16 G. Lippert, J. Dąbrowski, T. Schroeder, M. A. Schubert, Y. Yamamoto, F. Herziger, J. Maultzsch, J. Baringhaus, C. Tegenkamp, M. C. Asensio, J. Avila and G. Lupina, *Carbon*, 2014, **75**, 104–112.

17 J. M. Garcia, U. Wurstbauer, A. Levy, L. N. Pfeiffer, A. Pinczuk, A. S. Plaut, L. Wang, C. R. Dean, R. Buizza, A. M. Van

Der Zande, J. Hone, K. Watanabe and T. Taniguchi, *Solid State Commun.*, 2012, **152**, 975–978.

18 S. K. Jerng, D. S. Yu, Y. S. Kim, J. Ryou, S. Hong, C. Kim, S. Yoon, D. K. Efetov, P. Kim and S. H. Chun, *J. Phys. Chem. C*, 2011, **115**, 4491–4494.

19 U. Wurstbauer, T. Schiros, C. Jaye, A. S. Plaut, R. He, A. Rigosi, C. Gutiérrez, D. Fischer, L. N. Pfeiffer, A. N. Pasupathy, A. Pinczuk and J. M. Garcia, *Carbon*, 2012, **50**, 4822–4829.

20 S. Wang, L. Fernandes dos Santos, U. Wurstbauer, L. Wang, L. N. Pfeiffer, J. Hone, J. M. Garcia and A. Pinczuk, *Solid State Commun.*, 2014, **189**, 15–20.

21 M. Zhou, F. L. Pasquale, P. A. Dowben, A. Boosalis, M. Schubert, V. Darakchieva, R. Yakimova, L. Kong and J. A. Kelber, *J. Phys.: Condens. Matter*, 2012, **24**, 072201.

22 G. Lippert, J. Dabrowski, Y. Yamamoto, F. Herziger, J. Maultzsch, J. Baringhaus, C. Tegenkamp, M. C. Lemme, W. Mehr and G. Lupina, *Phys. Status Solidi B*, 2012, **249**, 2507–2510.

23 A. S. Plaut, U. Wurstbauer, A. Pinczuk, J. M. Garcia and L. N. Pfeiffer, *Appl. Phys. Lett.*, 2013, **102**, 241905.

24 Z. Liu, J. Tang, C. Kang, C. Zou, W. Yan and P. Xu, *Solid State Commun.*, 2012, **152**, 960–963.

25 M. Garnica, M. Schwarz, J. Ducke, Y. He, F. Bischoff, J. V. Barth, W. Auwärter and D. Stradi, *Phys. Rev. B*, 2016, **94**, 155431.

26 A. S. Plaut, U. Wurstbauer, S. Wang, A. L. Levy, L. Fernandes dos Santos, L. Wang, L. N. Pfeiffer, K. Watanabe, T. Taniguchi, C. R. Dean, J. Hone, A. Pinczuk and J. M. Garcia, *Carbon*, 2017, **114**, 579–584.

27 J. Lee, V. Varshney, J. Park, B. L. Farmer and A. K. Roy, *Nanoscale*, 2016, **8**, 9704–9713.

28 M. S. Driver, J. D. Beatty, O. Olanipekun, K. Reid, A. Rath, P. M. Voyles and J. A. Kelber, *Langmuir*, 2016, **32**, 2601–2607.

29 S. Balendhran, S. Walia, H. Nili, S. Sriram and M. Bhaskaran, *Small*, 2014, **11**, 640–652.

30 F.-f. Zhu, W.-j. Chen, Y. Xu, C.-l. Gao, D.-d. Guan, C.-h. Liu, D. Qian, S.-C. Zhang and J.-f. Jia, *Nat. Mater.*, 2015, **14**, 1020–1025.

31 M. E. Dávila, L. Xian, S. Cahangirov, A. Rubio and G. L. Lay, *New J. Phys.*, 2014, **16**, 095002.

32 A. J. Mannix, X.-F. Zhou, B. Kiraly, J. D. Wood, D. Alducin, B. D. Myers, X. Liu, B. L. Fisher, U. Santiago, J. R. Guest, M. J. Yacaman, A. Ponce, A. R. Oganov, M. C. Hersam and N. P. Guisinger, *Science*, 2015, **350**, 1513–1516.

33 B. Feng, J. Zhang, Q. Zhong, W. Li, S. Li, H. Li, P. Cheng, S. Meng, L. Chen and K. Wu, *Nat. Chem.*, 2016, **8**, 563–568.

34 P. Wu, Y. Zhang, P. Cui, Z. Li, J. Yang and Z. Zhang, *Phys. Rev. Lett.*, 2015, **114**, 216102.

35 E. Loginova, N. C. Bartelt, P. J. Feibelman and K. F. McCarty, *New J. Phys.*, 2008, **10**, 093026.

36 H. Tetlow, J. Posthuma de Boer, I. J. Ford, D. D. Vvedensky, J. Coraux and L. Kantorovich, *Phys. Rep.*, 2014, **542**, 195–295.

37 S. Nie, A. L. Walter, N. C. Bartelt, E. Starodub, A. Bostwick, E. Rotenberg and K. F. McCarty, *ACS Nano*, 2011, **5**, 2298–2306.

38 S. Nie, W. Wu, S. Xing, Q. Yu, J. Bao, S. shem Pei and K. F. McCarty, *New J. Phys.*, 2012, **14**, 093028.

39 A. Zangwill and D. D. Vvedensky, *Nano Lett.*, 2011, **11**, 2092–2095.

40 H. Chen, W. Zhu and Z. Zhang, *Phys. Rev. Lett.*, 2010, **104**, 186101.

41 E. Loginova, N. C. Bartelt, P. J. Feibelman and K. F. McCarty, *New J. Phys.*, 2009, **11**, 063046.

42 S. Riikonen, A. V. Krasheninnikov, L. Halonen and R. M. Nieminen, *J. Phys. Chem. C*, 2012, **116**, 5802–5809.

43 L. Zhong, J. Li, Y. Li, H. Lu, H. Du, L. Gan, C. Xu, S. W. Chiang and F. Kang, *J. Phys. Chem. C*, 2016, **120**, 23239–23245.

44 L. Xu, Y. Ma, Z. Wu, B. Chen, Q. Yuan and W. Huang, *J. Phys. Chem. C*, 2012, **116**, 4167–4174.

45 L. Xu, Y. Jin, Z. Wu, Q. Yuan, Z. Jiang, Y. Ma and W. Huang, *J. Phys. Chem. C*, 2013, **117**, 2952–2958.

46 S. Lizzit and A. Baraldi, *Cat. Tod.*, 2010, **154**, 68–74.

47 S. Lizzit, G. Zampieri, L. Petaccia, R. Larciprete, P. Lacovig, E. D. L. Rienks, G. Bihlmayer, A. Baraldi and P. Hofmann, *Nat. Phys.*, 2010, **6**, 345–349.

48 P. Lacovig, M. Pozzo, D. Alfè, P. Vilmercati, A. Baraldi and S. Lizzit, *Phys. Rev. Lett.*, 2009, **103**, 166101.

49 H. Tetlow, J. Posthuma de Boer, I. J. Ford, D. D. Vvedensky, D. Curcio, L. Omiciuolo, S. Lizzit, A. Baraldi and L. Kantorovich, *Phys. Chem. Chem. Phys.*, 2016, **18**, 27897–27909.

50 H. Tetlow, D. Curcio, A. Baraldi and L. Kantorovich, *Phys. Chem. Chem. Phys.*, 2018, doi:10.1039/c7cp07526j.

51 H. Hattab, A. N'Diaye, D. Wall, G. Jnawali, J. Coraux, C. Busse, R. Van Gastel, B. Poelsema, T. Michely, F.-J. Meyer Zu Heringdorf and M. Horn-Von Hoegen, *Appl. Phys. Lett.*, 2011, **98**, 141903.

52 X. Feng, S. Maier and M. Salmeron, *J. Am. Chem. Soc.*, 2012, **134**, 5662–5668.

53 A. Abrami, M. Barnaba, L. Battistello, A. Bianco, B. Brena, G. Cautero, Q. H. Chen, D. Cocco, G. Comelli, S. Contrino, F. DeBona, S. Di Fonzo, C. Fava, P. Finetti, P. Furlan, A. Galimberti, A. Gambitta, D. Giuressi, R. Godnig, W. Jark, S. Lizzit, F. Mazzolini, P. Melpignano, L. Olivi, G. Paolucci, R. Pugliese, S. N. Qian, R. Rosei, G. Sandrin, A. Savoia, R. Sergo, G. Sostero, R. Tommasini, M. Tudor, D. Vivoda, F. Wei and F. Zanini, *Rev. Sci. Instrum.*, 1995, **66**, 1618–1620.

54 A. Baraldi, G. Comelli, S. Lizzit, M. Kiskinova and G. Paolucci, *Surf. Sci. Rep.*, 2003, **49**, 169 – 224.

55 S. Doniach and M. Sunjic, *J. Phys. C*, 1970, **3**, 285–291.

56 D. Shirley, *Phys. Rev. B*, 1972, **5**, 4709–4714.

57 M. Bianchi, D. Cassese, A. Cavallin, R. Comin, F. Orlando, L. Postregna, E. Golfetto, S. Lizzit and A. Baraldi, *New J. Phys.*, 2009, **11**, 063002.

58 F. Presel, C. A. Tache, H. Tetlow, D. Curcio, P. Lacovig, L. Kantorovich, S. Lizzit and A. Baraldi, *J. Phys. Chem. C*, 2017, **121**, 11335–11345.

59 A. N'Diaye, J. Coraux, T. Plasa, C. Busse and T. Michely, *New J. Phys.*, 2008, **10**, 043033.
60 A. T. N'Diaye, S. Bleikamp, P. J. Feibelman and T. Michely, *Phys. Rev. Lett.*, 2006, **97**, 215501.
61 C. Busse, P. Lazić, R. Djemour, J. Coraux, T. Gerber, N. Atodiresei, V. Caciuc, R. Brako, A. N'Diaye, S. Blügel, J. Zegenhagen and T. Michely, *Phys. Rev. Lett.*, 2011, **107**, 036101.
62 J. Hutter, M. Iannuzzi, F. Schiffmann and J. VandeVondele, *Wiley Interdiscip. Rev.: Comput. Mol. Sci.*, 2013, **4**, 15–25.
63 S. Goedecker, M. Teter and J. Hutter, *Phys. Rev. B*, 1996, **54**, 1703–1710.
64 J. P. Perdew, K. Burke and M. Ernzerhof, *Phys. Rev. Lett.*, 1996, **77**, 3865–3868.
65 S. Grimme, *J. Comput. Chem.*, 2006, **27**, 1787–1799.
66 J. VandeVondele and J. Hutter, *J. Chem. Phys.*, 2007, **127**, 114105.
67 G. Henkelman, B. P. Uberuaga and H. Jónsson, *J. Chem. Phys.*, 2000, **113**, 9901–9904.
68 T. Balasubramanian, J. N. Andersen and L. Walldén, *Phys. Rev. B*, 2001, **64**, 205420.
69 M. P. Seah and W. A. Dench, *Surf. Interface Anal.*, 1979, **1**, 2–11.
70 P. Hofmann, C. Søndergaard, S. Agergaard, S. V. Hoffmann, J. E. Gayone, G. Zampieri, S. Lizzit and A. Baraldi, *Phys. Rev. B*, 2002, **66**, 245422.
71 M. Pozzo, D. Alfè, P. Lacovig, P. Hofmann, S. Lizzit and A. Baraldi, *Phys. Rev. Lett.*, 2011, **106**, 135501.
72 E. Miniussi, M. Pozzo, T. Menteş, M. Niño, A. Locatelli, E. Vesselli, G. Comelli, S. Lizzit, D. Alfè and A. Baraldi, *Carbon*, 2014, **73**, 389–402.
73 B. Wang, S. Günther, J. Wintterlin and M.-L. Bocquet, *New J. Phys.*, 2010, **12**, 043041.
74 A. Martín-Recio, C. Romero-Muñiz, A. J. Martínez-Galera, P. Pou, R. Pérez and J. M. Gómez-Rodríguez, *Nanoscale*, 2015, **7**, 11300–11309.
75 J. W. May, *Surf. Sci.*, 1969, **17**, 267 – 270.
76 P. Merino, M. Švec, A. L. Pinardi, G. Otero and J. A. Martín-Gago, *ACS Nano*, 2011, **5**, 5627–5634.
77 N. Ferralis, K. Pussi, S. E. Finberg, J. Smerdon, M. Lindroos, R. McGrath and R. D. Diehl, *Phys. Rev. B*, 2004, **70**, 245407.
78 H. Kazi, Y. Cao, I. Tanabe, M. S. Driver, P. A. Dowben and J. A. Kelber, *Mater. Res. Express*, 2014, **1**, 035601.
79 A. Y. Cho, *J. Vac. Sci. Technol.*, 1979, **16**, 275–284.